A Combined 3-D Geometric and Magnetic Modeling Approach of Coils in Air-Cored Resonant Induction Machines

Zhao Jin
Department of Electrical and Electronic Engineering
The University of Manchester
Manchester, U.K.
zhao.jin@manchester.ac.uk

Rajesh P. Deodhar
IMRA Europe S.A.S.
UK Research Centre
Brighton, U.K.
rd@imra-ukrc.com

Matteo F. Iacchetti
Department of Energy, Politecnico di Milano, IT
Department of Electrical and Electronic Engineering
The University of Manchester
Manchester, U.K.
matteo.iacchetti@manchester.ac.uk

Yoshiyuki Komi
Aisin Corporation
Kariya, Japan
yk@imra-ukrc.com

Chiaki Umemura
Aisin Corporation
Kariya, Japan
cu@imra-ukrc.com

Alexander C. Smith
Department of Electrical and Electronic Engineering
The University of Manchester
Manchester, U.K.
sandy.smith@manchester.ac.uk

Ahmad Anad Abduallah
IMRA Europe S.A.S.
UK Research Centre
Brighton, U.K.
aa@imra-ukrc.com

Abstract—**Because of the air-cored and toothless structure, ACRIMs usually have coils with flat cross-sections and need 3-D inductance evaluation. Since the precision in geometry modeling is vital to the inductance-estimation accuracy, a combined geometry modeling and inductance calculation method is proposed. The coil geometry construction process can handle non-circular cross-section and complex coil shapes, it generates a single- or multi-filament model ready for analytic inductance calculation and coordinates information for 3-D FEA modeling. Based on the closed-form solutions for the mutual inductance of two straight segments placed at any orientation in 3-D, the filament-level, conductor-level, coil-level and winding-level inductances can be calculated, the entire calculation procedure is fast, accurate and avoids numerical singularities so is suitable to be incorporated into an optimization program. Good correlation is confirmed in validation against 3-D FEA results on an air-cored resonant induction machine design.**

Keywords—3-D inductance evaluation, air-cored machines, complex coil geometry construction, closed-form expressions, multi-filament method.

I. INTRODUCTION

Air-cored resonant induction machines (ACRIMs) remove the magnetic core and offer many favorable features like reduced mass, eliminating saturation issues thus no iron losses, good overload capability, low inertia, no cogging torque, and the potential to operate under a square-wave modulation. They are promising for high-speed and high-power-density applications. Though the magnetic loading usually drops in air-cored induction machines (IMs), the capacitors in ACRIMs can partially or totally cancel out the machine reactance in an operating range and allow ACRIM windings to carry more current, so the electric loading is boosted and the torque capability is improved [1]. Also, for a required torque and speed demand, the supply voltage is reduced compared to pure air-cored IMs [2]. Several capacitor tuning criteria of ACRIMs have been investigated but the design aspect of ACRIM has not been fully studied especially for its winding inductance estimation. A 2-D current-sheet model of ACRIMs ignoring the excitation thickness is constructed in [1], a 2-D model assuming infinite-long conductors with round cross-sections is built in [3], and 2-D finite element analyses (FEA) are used in [4] and [5], none of them captures the important 3-D feature of air-cored windings. In air-cored machines, the magnetic field is inherently 3-D, and requires 3D analysis.

3-D FEA can be a way to numerically evaluate 3-D inductances, but it has two main issues, especially when incorporating into a design optimization program, one is the high computational costs and the other is the detailed geometry modeling, particularly for the end-winding parts. 3-D FEA was used to calculate the inductance and was embedded into an optimisation program for designing an ironless axial-flux permanent-magnet machine (AFPM) in [6], the genetic algorithm is applied for quicker convergence thus fewer number of evaluations are needed and the time reported to find the optimal design on a high-performance workstation is 29 hours. Another multi-objective optimization for designing a coreless AFPM was carried out in [7]; though a two-level algorithm is implemented to substantially reducing the number of evaluations, 120 3-D FEA simulations was still needed to plot the Pareto front. It can be seen that the computational costs of 3-D FEA are very high and usually make it inefficient for an optimization procedure. Also, the geometry of windings needs to be updated automatically from design to design in the optimization, so the entire 3-D winding shape needs to be defined in a parametric routine. Unlike the concentrated or "tooth"-wound coils used in [6] and [7], conductor clashing can happen in 3-D geometry generation for complex winding shapes like hand-wound lap windings. This prevents the definition of individual coils so is not tolerated in 3-D FEA.

Apart from FEA methods, there are other analytic methods to calculate 3-D inductances. Expressions to calculate the 3-D

magnetic field produced by a bulk conductor with rectangular cross-section in free space are derived in [8], however, it involves numerical evaluation of Jacobi elliptic functions and the field solution still needs to be integrated to derive the inductance value, which adds to the computational burden. Neumann integrals are applied in [9] to calculate the end-winding reactance of an IM, and one coil end is represented by one filament locating at its center, but direct implementation of Neumann integrals brings two issues: there is a trade-off between element size and the solution accuracy; and a weak numerical singularity arises when two segments intersect. Closed-form solutions based on Neumann integrals are derived in [10] and [11] for inductances of two segments placed at different orientations and of coils in special shapes, these expressions help to resolve singularity issues caused by numerical quadrature, however, coils are still represented by their central filaments, which works well for conductors with round cross-sections, but is not so accurate for adjacent conductors with non-circular such as flat cross-sections.

This paper presents a 3-D geometric modeling method and a 3-D winding inductance calculation method for ACRIMs. A general geometry construction method for complex coil shapes is presented first; the coil is characterized by a sequence of cross-sections, which can be calculated directly or drawn by geometry transformations, then vertices of filaments are located using local coordinate systems attached to these cross-sections. Connecting corresponding vertices forms a filament and multiple filaments can be arranged inside the coil to reflect the shape and change in cross-sections and the twisting and bending in coils. Second, the calculation for mutual inductance of two segments placed at any orientation using closed-form solutions of Neumann integrals is explained, and segment-level inductances are then collected to calculated the filament-level, conductor-level, coil-level and winding level inductances. Finally, the proposed method combining geometry modeling and inductance calculation is validated by a 3-D FEA.

II. A GENERAL COIL GEOMETRY MODELING METHOD

A. Coil Geometry Construction

1) Building Cross-Sections

A coil is firstly characterized by a sequence of its cross-sections. For each cross-section, it is seen as a closed 2-D polygon and is described by the positions of its vertices in the form of a matrix, $\mathbf{M}_{Cs}$. For example, a cross-section with n_{Csv} vertices is written in the form of an n_{Csv}-by-3 matrix in which every row stores the coordinates of one vertex, so the number of rows is equal to the number of vertices, and the three columns correspond to the x, y, z coordinates of the vertex. There can be variations in the cross-section shape along the coil, so the size of the cross-section matrix, i.e., the number of rows in $\mathbf{M}_{Cs}$, can also be varied. Cross-sections with n_{Csv1} and n_{Csv2} vertices respectively are written in the matrix form in $\mathbf{M}_{Cs,1}$ and $\mathbf{M}_{Cs,2}$ as shown in Fig. 1.

For a straight conductor with unvarying cross-section, it can be simply represented by two cross-sections at both ends. For a conductor with bending or twisting however, it needs to be approximated by multiple cross-sections at different positions along the coil spine. Cross-sections can be drawn by direct calculation and by 3-D geometric transformations. The direct calculation refers to calculating the cross-section vertices directly using measurable machine geometry parameters, it is usually applied to cross-sections parallel to

the xy or yz or xz plane when the calculation reduces to a 2-D problem and the vertices are easier to calculate, it is useful in defining the initial cross-section shape and the axial-winding cross-sections. However, for conductors involving twisting and bending such as the coil ends, 3-D geometric transformations are often invoked: based on an existing cross-section, operations like translation along a 3-D spine and rotation around an arbitrary 3-D axis can quickly put the cross-section in place. Also, operations like reflection over a plane can conveniently complete the coil if symmetry exists. All of these operations are essentially carried out by multiplying the corresponding 3-D transformation matrix $\mathbf{T}$, such as the translation transformation matrix $\mathbf{T}_{trans}$ or rotation transformation matrix $\mathbf{T}_{rot}$, to a cross-section matrix $\mathbf{M}_{Cs}$, shown as $\mathbf{M}_{Cs,i}$ and $\mathbf{M}_{Cs,j}$ in Fig. 1 [12].The collection of all the cross-section matrices in a coil is denoted as $\mathbb{C}_{Cs}$, and $\mathbb{C}_{Cs} = \{\mathbf{M}_{Cs,1}, \mathbf{M}_{Cs,1}, \ldots, \mathbf{M}_{Cs,n_{Cs}}\}$, which contains n_{Cs} cross-sections.

2) Locating Filament Vertices

The next step after placing all cross-sections is to locate the "punctures" on them where the filaments will penetrate through, connecting corresponding puncture points over cross-sections in sequence to form a continuous filament. The positions of these points are determined using a local coordinate system attached to each cross-section. The local coordinate system has two base vectors, denoted as $\mathbf{u}$ and $\mathbf{v}$. For a rectangular cross-section particularly, a local Cartesian coordinate system can be established by choosing its two adjacent edges as the two axes. For a cross-section has n_{Csp} points on it, the ith point, P_i, is assumed to have a local coordinate of $P_{i,loc} = (a_i, b_i)$, then the position of P_i in the global coordinate system $P_{i,glo}$, can be easily calculated as $a_i\mathbf{u} + b_i\mathbf{v} + \mathbf{t}$, where $\mathbf{t}$ is the translation vector pointing from the global origin to the local origin. The information of all points on this cross-section can be written in a n_{Csp}-by-3 matrix, $\mathbf{M}_{Pt}$, in which every row stores the global x, y, z coordinates of one point on the cross-section. The collection of all the point matrices is denoted as $\mathbb{C}_{Pt}$. and $\mathbb{C}_{Pt} = \{\mathbf{M}_{Pt,1}, \mathbf{M}_{Pt,2}, \ldots, \mathbf{M}_{Cs,n_{Fa}}\}$, where n_{Fa} is the number of cross-section, or faces, with puncture points defined, as shown in Fig. 1.

3) Forming Filaments

The final step is the filament formation. One filament can be composed of only one straight filamentary segment, or several straight filamentary segments connected together. A filament does not have to be a closed polygon. Connecting the corresponding points on two cross-sections forms one segment in a filament. Clearly, smooth bending and twisting of coils are discretized by several straight segments because they are firstly approximated using multiple cross-sections. Each filament composed of n_v vertices, can be recorded using an n_v-by-3 matrix, $\mathbf{M}_{Fil}$, in which each row stores the x, y, z coordinates of one vertex. Finally, the collection of all filaments in a coil is written as a set of matrices, denoted as $\mathbb{C}_{Fil}$, as shown in . $\mathbb{C}_{Fil} = \{\mathbf{M}_{Fil,1}, \mathbf{M}_{Fil,2}, \ldots, \mathbf{M}_{Cs,n_{Fil}}\}$, where n_{Fil} is the total number of filaments.

The number of filaments in different parts of a coil does not need to be the same. However, in a simpler case that a coil is constructed with all filaments follow the same complete path along the coil spine, connecting the ith points on all cross-sections in sequence by straight segments forms the ith filament, and the number of vertices on every filament is equal to the number of cross-sections, i.e., $n_v = n_{Cs}$; the number of filaments is equal to the number of points on every cross-

section, i.e., $n_{Fil} = n_{Csp}$. The general coil geometry construction process is illustrated in Fig. 1.
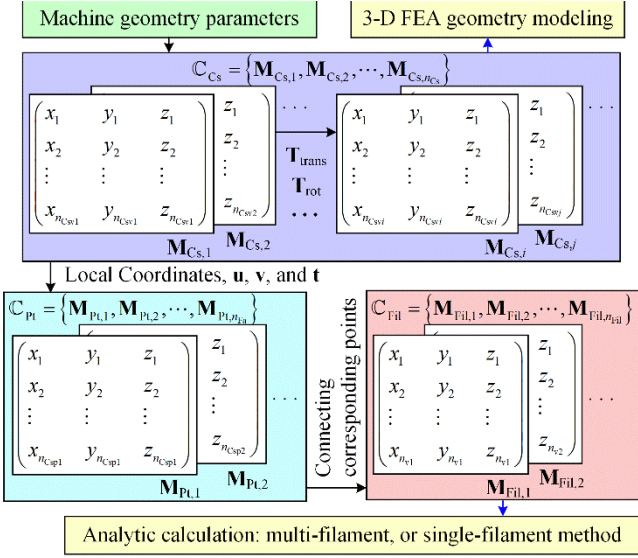

Fig. 1. The general coil geometry construction process.

B. Example: Coisl in a Lap Winding

This section presents the geometry construction process of a coil with rectangular cross-section in a single-layer lap winding. Unlike coils with round cross-sections, the rotation in rectangular cross-section caused by bending and twisting needs to be handled properly to avoid cross-section mismatch. One final analytic coil shape is shown in Fig. 2.
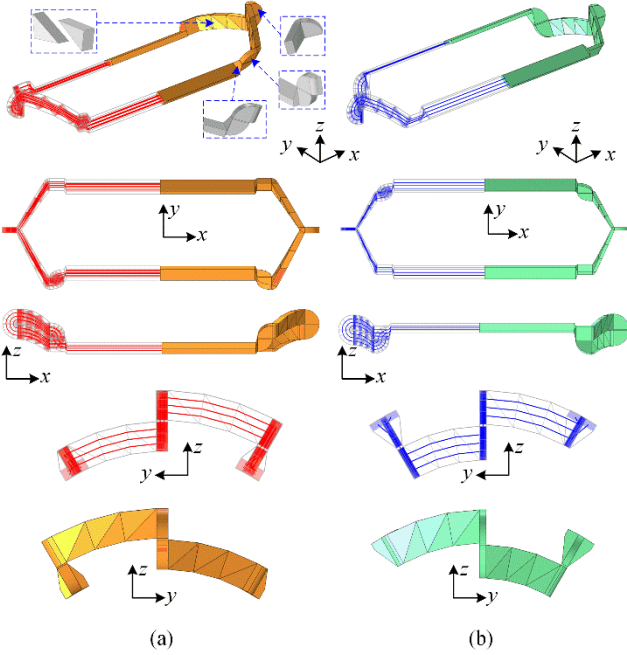

Fig. 2. Analytic coils and their corresponding 3-D FE coils. (a) shows the stator coil and (b) shows the rotor coil. For analytic coils: red and blue lines represent the filaments inside; silver lines outline the conductor edges, red and blue faces illustrate all cross-sections. 3-D FE coils are in yellow and green, which are built directly using analytic calculated coordinates.

The axial part conductor, denoted as $\mathbb{A}$, is a rectangular cuboid so it can be simply characterized by its start and end cross sections. Placing the start cross-section parallel to the yz plane, its coordinates can be calculated directly using machine geometry parameters such as the baseline circle radius, axial

coil-side width and depth, then its end cross-section can be obtained by a translation along the x axis.

Since the coil may have different cross-section width and depth in the end-region, a quadrilateral frustum is attached to the end of the axial part for cross-section transition, denoted as $\mathbb{AE}$ part. As shown in Fig. 3(a), the end face of $\mathbb{A}$, $ABCD$, is transformed to $EFGH$ with different depth and width, both $ABCD$ and $EFGH$ are rectangles and parallel to the yz plane.
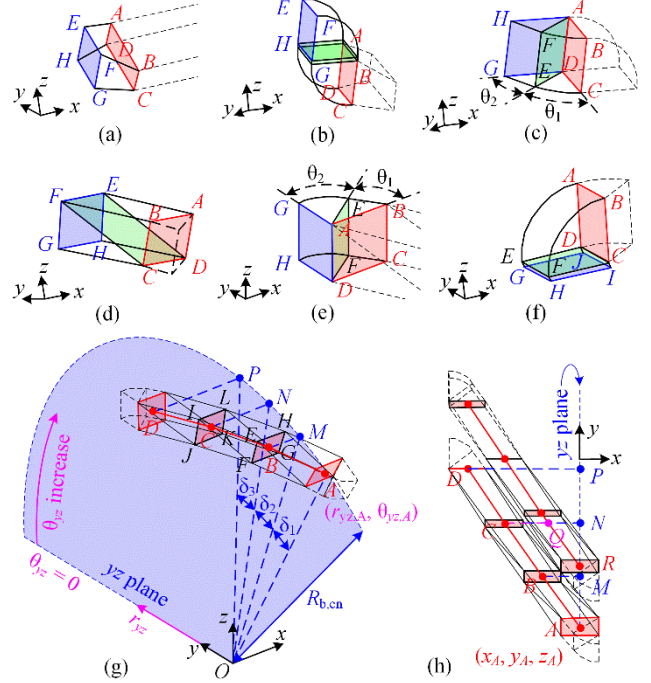

Fig. 3. Detailed Geometry of different parts in the analytic coil. (a) Part $\mathbb{AE}$. (b) Part $\mathbb{JA}$. (c) Part $\mathbb{JE}$. (d), (g) and (h) are Part $\mathbb{E}$. (e) Part $\mathbb{JN}$. (f) Part $\mathbb{N}$.

To avoid coil-end clashing, the two-layer end-winding arrangement is adopted [13], [14]. A step is connected right after $\mathbb{AE}$ which joins the axial and end parts, denoted as $\mathbb{JA}$. As shown in Fig. 3(b), the end cross-section of $\mathbb{AE}$, i.e., $ABCD$, is firstly rotated by $\theta_1 = \pi/2$ around axis BA, then the resultant cross-section is lifted by a translation in radial direction to form a "neck" which creates a clearance between the upper and lower layers of coil ends. Finally, the end face of neck is rotated around axis HG by $\theta_2 = \pi/2$ to $EFGH$. $\mathbb{JA}$ can raise or lower the axial cross-section in the radial direction for a coil-end bent outwards or inwards without changing its shape. Also, depending on the end-winding arrangement and end cross-section depth, the neck may not be necessary and θ_1, θ_2 can be smaller than $\pi/2$.

The end-winding is assumed to have a helix spine, and the end-winding angle is defined as φ, so the angle between the machine shaft, i.e., the cylinder axis, and the tangential line at any point on the spine is always $(\pi/2-\varphi)$. A joint is used before the end part to form the bend, denoted as $\mathbb{JE}$, as shown in Fig. 3(c). The end cross-section of $\mathbb{JA}$, $ABCD$, which is parallel to the yz plane, is firstly rotated by $\theta_1 = \pi/2-\varphi$ around axis AD, then the normal vector of the resultant face $ADEF$, i.e., the coil spine, has an angle $(\pi/2-\varphi)$ to the machine shaft, i.e., the x axis. This step completes the bending, but the position of $ADEF$ can make following steps difficult to construct solid geometry since none of its edges is parallel to any axis. Therefore, another cross-section is found by cutting the coil using a plane parallel to x axis along AD, the resultant face is shown by

ADGH in Fig. 3(c). In practice, *HG* can be obtained by translating *AD* along x axis by $w_{en}/\cos(\varphi)$, where w_{en} is the coil-end cross-section width, i.e., |*AB*| in Fig. 3(c). *AFH-DEG* is a triangular prism and $\angle HAF = \angle GDE = \varphi$. Though *ADGH* is not perpendicular to the spine, its edges *AH* and *DG* are parallel to the x axis, which is helpful in later end-part solid formation.

The end-winding part, denoted as $\mathbb{E}$, are constructed using cross-sections in radial direction and parallel to x axis. As shown in Fig. 3(g) and (h), faces *EFGH* and *IJKL* are both parallel to x axis and cross the origin point *O*. The projection of upper-layer end winding in yz plane has a baseline radius $R_{b,en}$; the helix radius set for entire end-winding is R_e, which is usually chosen as the mean radius of upper and lower end layers. The central point on the end face of $\mathbb{JE}$ is *A*, its Cartesian coordinates is (x_A, y_A, z_A), and its projection on yz plane in polar coordinates is $(r_{yz,A}, \theta_{yz,A})$, then the coordinates of point *E*, *F*, *G* and *H*, for example, can be easily calculated as $x_E = x_F = x_A - R_e\delta_1\tan(\varphi) - w_{en}/[2\cos(\varphi)]$; $x_G = x_H = x_A - R_e\delta_1\tan(\varphi) + w_{en}/[2\cos(\varphi)]$; $y_E = y_H = (R_{b,en}+d_{en}/2)\cos(\theta_{yz,A}-\delta_1)$; $y_F = y_G = (R_{b,en}-d_{en}/2)\cos(\theta_{yz,A}-\delta_1)$; $z_E = z_H = (R_{b,en}+d_{en}/2)\sin(\theta_{yz,A}-\delta_1)$; $z_F = z_G = (R_{b,en}-d_{en}/2)\sin(\theta_{yz,A}-\delta_1)$, where d_{en} is the end-winding coil-side depth. As a result, *EH* ∥ *FG* ∥ *SV* ∥ *TU*. Since *EF* ∦ *ST* and *GH* ∦ *UV*, a splitting face *ETUH* is inserted to form two triangular prisms *EFT-HGU* and *ETS-HUV* back-to-back to resolve the cross-section twisting, as shown in Fig. 3(c). Triangular prisms *EFI-HGL* and *IFJ-LGK* in Fig. 3(g) are built in the same way. Fig. 3(h) shows the end-windings of two adjacent coils, it can be observed from the geometry relation that one criterion to avoid end-winding clashing is |*CQ*| > $w_{en}\cos(\varphi)$, considering /*CQ*/ = $R_e|\theta_{yz,A} - \theta_{yz,R}|\tan(\varphi)$, and $|\theta_{yz,A} - \theta_{yz,R}|$ is the angular difference between the projection of two adjacent axial conductors in yz plane, i.e., the "slot" angle α_{ax}, the criterion can be re-written as $\tan(\varphi)\sec(\varphi) > w_{en}/(\alpha_{ax}R_e)$.

The final cross-section of $\mathbb{E}$ part, as shown by *ABCD* in Fig. 3(e), is set as parallel to the zx plane, and its distance to the zx plane is the half coil-end cross-section width. Then the cross-section perpendicular to the coil spine is reverted by translating *AD* by a distance w_{en} with an angle $\theta_1 = \varphi$, i.e., the end-winding angle. The resultant face *ADFE* is then rotated around axis *DA* by $(\pi/2-\varphi)$ to form *ADHG* parallel to yz plane. This step forms the joint between the end and nose parts, denoted as $\mathbb{JN}$. The nose part, $\mathbb{N}$, is subsequently obtained by rotating the end face of $\mathbb{JN}$, i.e., *ABCD* in Fig. 3(f), by $\pi/2$, the resultant face *CDEF* is in xy plane and is connected to the nose part on the other half end-winding by a parallelepiped *EFCD-GHIJ*, which is also used to tolerate and compensate for the potential displacement between upper and lower end-layers in practice.

The calculated cross-section coordinates are directly fed into 3-D FEA since they are all vertices of real solids rather than imaginary object, and one 3-D FE coil is constructed as shown in Fig. 2. The analytic stator coil in Fig. 2 has 3-by-2 uniformly distributed filaments inside. A constant local-coordinate matrix is defined for all cross-sections, which stores the local Cartesian coordinates of one point in each row and is 6-by-2 in size. Base vector **u** is always set as the longer edge of the cross-section and **v** as the shorter edge, so local coordinates (1/4, 1/3) always refers to a position at 1/4 of the longer edge and 1/3 of the shorter edge. According to the local coordinates, three columns of filaments are distributed evenly along the longer edge with each column containing two

filaments, distributed uniformly along shorter edge. Finally, filaments are generated by connecting the corresponding points on every cross-section.

III. MAGNETIC MODELING AND INDUCTANCE CALCULATION

A. Mutual Inductance of Two Straight Segments Placed at Any Orientation in 3-D

The ACRIM winding inductances are calculated from the coil self and coil-to-coil mutual inductances, while the coil-level inductances are calculated based on the conductor-to-conductor or filament-to-filament inductance. The filament-level inductance is obtained by collecting the segment-to-segment inductances, so the mutual inductance between two filamentary segments placed at any orientation in 3-D is the basis for the whole calculation.

The first step is to determine the spatial relation of two straight segments so correct equations can be applied. Fig. 4 shows two straight filamentary segments *AB* and *CD* placed arbitrarily in 3-D, their unit-direction vectors are $\mathbf{m}_1$ and $\mathbf{m}_2$, respectively; the cross product of $\mathbf{m}_1$ and $\mathbf{m}_2$ is $\mathbf{w}$, i.e., $\mathbf{w} = \mathbf{m}_1 \times \mathbf{m}_2$; the normal vectors of planes *ABC* and *ABD* are $\mathbf{n}_1$ and $\mathbf{n}_2$, respectively; |*AB*|, |*AC*|, |*AD*|, |*CD*|, |*CB*| and |*BD*| are distances between every two vertices. All these vectors and distances can be calculated using the coordinates of the four vertices *A*, *B*, *C* and *D* and they are needed in the spatial-relation determination.
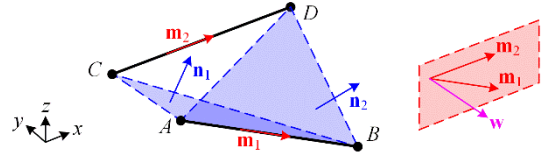

Fig. 4. Two straight filamentary segments placed at any orientation in 3-D.

4) Mutual Inductance of Two Parallel Segments

When $\mathbf{m}_1 \parallel \mathbf{m}_2$, *AB* and *CD* are in parallel. The closed-form solution for the mutual inductance of unequal parallel filaments, as shown in (7) in the Appendix, needs to be applied. The expression is denoted as Exp-M_{pa} in the main text for simplicity. It is worth mentioning that, whether $\mathbf{m}_1$ and $\mathbf{m}_2$ are parallel is usually determined using their dot product, i.e., $\mathbf{m}_1 \cdot \mathbf{m}_2 = 0$ means *AB* and *CD* are in parallel otherwise they are unparallel, but in practice, a very small tolerance, ϵ, needs to be used to compensate for the residual in numerical calculation, i.e., the criterion becomes $|\mathbf{m}_1 \cdot \mathbf{m}_2| < \epsilon$ ($\epsilon > 0$).

Also, there are special cases needs to be checked. It can be noticed that, if term d in (7) is 0, Exp-M_{pa} will be trapped into a singularity. Specifically, there can be two cases. The first case is when the two segments are entirely or partially overlapping, as shown in Fig. 5(a) and (b), *AB* and *CD* are still in parallel but the mutual inductance between them goes to infinity. As a result, segment overlapping, both entirely or partially, needs to be avoided from the geometry modeling. The second case is when *AB* and *CD* are collinear without meeting and overlapping, as shown in Fig. 5(c). A closed-form solution for mutual inductance of them can be easily derived using Neumann integrals for this particular situation.

In Fig. 5(c), the length of segments *AB* and *CD* are l_1 and l_2 respectively, the distance between their near ends, i.e., |*CB*|, is δ. The mutual inductance of two unequal collinear not-meeting filaments, $M_{pa\text{-}cl}$, is,

$$M_{\text{pa-cl}} = \frac{\mu_0}{4\pi} \int_{l_1} \int_{l_2} \frac{d\mathbf{x}_1 \cdot d\mathbf{x}_2}{|\mathbf{x}_1 - \mathbf{x}_2|}$$

$$= 10^{-7} (\delta \ln \delta - (l_1 + \delta) \ln(l_1 + \delta)$$
$$- (l_2 + \delta) \ln(l_2 + \delta) + (l_1 + l_2 + \delta) \ln(l_1 + l_2 + \delta)) \quad (1)$$

Where μ_0 is the vacuum permeability, $\mathbf{x}_1$ and $\mathbf{x}_2$ are the vectors pointing from the origin to the line elements $d\mathbf{x}_1$ and $d\mathbf{x}_2$ on *AB* and *CD*, respectively.
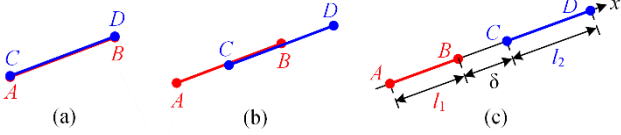

Fig. 5. Two parallel segments placed at special positions. (a) *AB* and *CD* are entirely overlap. (b) *AB* and *CD* are partially overlap. (c) *AB* and *CD* are collinear without meeting.

5) Mutual Inductance of Two Unparalel segments Meeting at One End

If *AB* and *CD* are unparallel, but they meet at one end, then they are in the same plane and the closed-form solution for mutual inductance between two unequal filaments meeting at one end needs to be applied, as shown in (8) in the Appendix. The expression is denoted as Exp-M_{mt}. Similarly, "meeting" is practically defined as: the distance between two ends on different segments is below a very small tolerance, ϵ. Since $l_1 + R > m_1$ and $m_1 + R > l_1$ in (8), Exp-M_{mt} does not encounter any singularity. It is clear that, when *AB* and *CD* are perpendicular to each other, the mutual inductance of them is 0.

6) Mutual Inductance of Two Unparallel But Coplannar Segments Without Two End-Points Meeting

When *AB* and *CD* are unparallel and not meeting at any end, then the vector $\mathbf{w} = \mathbf{m}_1 \times \mathbf{m}_2$ needs to be calculated, which is the cross product of the unit-direction vectors of the two segments. The reason to introduce $\mathbf{w}$ is because planes *ABC* or *ABD* may not always exist, for example, when one end of a segment lies on the other segment, or on the straight extension of the other segment, as shown in Fig. 6, then $\mathbf{n}_1$ or $\mathbf{n}_2$ can be unavailable. If any two of the three vectors $\mathbf{n}_1$, $\mathbf{n}_2$, $\mathbf{w}$ are in parallel, i.e., $\mathbf{n}_1 \| \mathbf{n}_2$ or $\mathbf{n}_1 \| \mathbf{w}$ or $\mathbf{n}_2 \| \mathbf{w}$, then *AB* and *CD* are still coplanar though not in parallel nor meeting at one end, the corresponding closed-form expression (9) as shown in Appendix needs to be applied, which is denoted as Exp-M_{cp}.
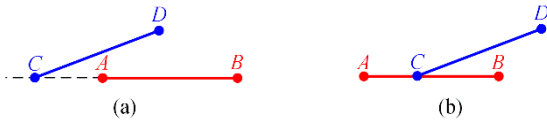

Fig. 6. (a) End point *C* is on the extension of *AB*. (b) End point *C* is on *AB*.

However, there are terms in (9) involving inverse hyperbolic tangent. It is known that, $\tanh^{-1}(\xi)$ is defined on a domain of $\xi \in (-1, 1)$, so (9) becomes unapplicable if the ξ fall outside this domain. According to the defined geometry and the triangle inequality in Fig. 11(a), there are always $R_1 + R_2 \geq m$, $R_1 + R_4 \geq l$, $R_3 + R_4 \geq m$ and $R_2 + R_3 \geq l$, but when $R_1 + R_2 = m$, or $R_1 + R_4 = l$, or $R_3 + R_4 = m$, or $R_2 + R_3 = l$, the argument applied to $\tanh^{-1}$ is 1 so (9) becomes invalid, which corresponds to the situation that one end of a segment lies on the other unparallel segment. This situation can be resolved by breaking the intersected segment at the intersection point and

using Exp-M_{mt} instead. As shown in Fig. 6(b), end point *C* is on segment *AB*. Direct implementation of Exp-M_{cp} causes singularity, so the mutual inductance of *AB* and *CD* can be calculated by breaking *AB* into two sub-segments *AC* and *CB*, then adding the mutual inductances of *AC* and *CD*, and *CB* and *CD*, i.e., $M_{\text{cp-ACB}}(AB, CD) = M_{\text{mt}}(AC, CD) + M_{\text{mt}}(CB, CD)$, where $M_{\text{cp-ACB}}(AB, CD)$ represents the mutual inductance of *AB* and *CD* when end point *C* is on segment *AB*, $M_{\text{mt}}(AC, CD)$ means calculating the mutual inductance of *AC* and *CD* using Exp-M_{mt}.

Except for the special case above, mutual inductance of other spatial relations under this circumstance can be computed directly using (9): either the two segments are crossing each other or they do not have any intersection at all, no singularity will be produced. Also, when the two segments are perpendicular to each other, regardless intersecting or not, the mutual inductance of them is 0, which can be given without calculation.

7) Mutual Inductance of Skew Segments

If *AB* and *CD* are unparallel and it is unable to find any two of the three vectors $\mathbf{n}_1$, $\mathbf{n}_2$, $\mathbf{w}$ in parallel, then *AB* and *CD* are not coplanar, i.e., *AC* and *CD* are skew. The closed-form expression for mutual inductance of skew segments, denoted as Exp-M_{sk}, is shown as (12) in Appendix. Since the spatial relation of the two segments has been restricted to skew, the expression can be directly applied and does not encounter singularity issues.

The entire procedure for mutual inductance calculation of two straight filamentary segments placed at any orientation in 3-D is summarized in Fig. 7.

B. Self and Mutual Inductances of Coils and Windings

The mutual inductance between two filaments composed of multiple sub-segments, $M_{\text{Fil-Fil}}$, can be calculated as

$$M_{\text{Fil-Fil}}(\text{Fil}_1, \text{Fil}_2) = \sum_{i=1}^{N_{\text{Seg,Fil1}}} \sum_{j=1}^{N_{\text{Seg,Fil2}}} M_{\text{Seg-Seg}}(\text{Seg}_i, \text{Seg}_j) \quad (2)$$

where $M_{\text{Seg-Seg}}(\text{Seg}_i, \text{Seg}_j)$ are the mutual inductance between two segments Seg_i and Seg_j; $N_{\text{Seg,Fil1}}$ and $N_{\text{Seg,Fil2}}$ are the number of segments in filaments Fil_1 and Fil_2 respectively.

One coil can be assumed to be composed of several conductors. The self-inductance of a conductor, L_{Cond}, can be calculated as

$$L_{\text{Cond}}(\text{Cond}_1) = \frac{1}{N_{\text{Fil}}^2} \sum_{i=1}^{N_{\text{Fil,Cond1}}} \sum_{j=1, j \neq i}^{N_{\text{Fil,Cond2}}} M_{\text{Fil-Fil}}(\text{Fil}_i, \text{Fil}_j) \quad (3)$$

where $N_{\text{Fil,cond}_1}$ is the number of filaments in the conductor Cond_1. The mutual inductance between two coils, $M_{\text{Cond-Cond}}$, can be calculated as

$$M_{\text{Cond-Cond}}(\text{Cond}_1, \text{Cond}_2) =$$
$$\frac{1}{N_{\text{Fil,Cond}_1} N_{\text{Fil,Cond}_2}} \sum_{i=1}^{N_{\text{Fil,Cond1}}} \sum_{j=1}^{N_{\text{Fil,Cond2}}} M_{\text{Fil-Fil}}(\text{Fil}_i, \text{Fil}_j) \quad (4)$$

where $N_{\text{Fil,cond}_1}$ and $N_{\text{Fil,cond}_2}$ are the number of filaments in conductors, Cond_1 and Cond_2, respectively. Both L_{Cond} and $M_{\text{Cond-Cond}}$ are known as the partial inductances since they may not complete a closed loop. The coil self and mutual inductances, i.e., the loop inductances, can be calculated by

summing partial inductances. More specifically, the coil self-inductance, L_{Coil}, can be calculated as

$$L_{Coil}(Coil_1) = \sum_{i=1}^{N_{Cond,Coil_1}} (L_{Cond}(Cond_i)$$
$$+ \sum_{j=1,\,j\neq i}^{N_{Cond,Coil_1}} M_{Cond\text{-}Cond}(Cond_i, Cond_j)) \quad (5)$$

where $N_{Cond,Coil_1}$ is the number of conductors in coil, $Coil_1$. The mutual inductance between two coils, $M_{Coil\text{-}Coil}$ is

$$M_{Coil\text{-}Coil}(Coil_1, Coil_2) =$$
$$\sum_{i=1}^{N_{Cond,Coil1}} \sum_{j=1}^{N_{Cond,Coil2}} M_{Cond\text{-}Cond}(Cond_i, Cond_j) \quad (6)$$

where $N_{Cond,Coil_1}$ and $N_{Cond,Coil_2}$ are the number of conductors in coils, $Coil_1$ and $Coil_2$, respectively.

The phase winding self and mutual inductances can be calculated by collecting the contribution of coil inductances. Periodicity and symmetry in three-phase winding layout can be invoked so that only mutual inductances of independent coil pairs are computed and repeated evaluations are eliminated, which further accelerates the calculation. The collection routine of phase inductances for single-layer lap-windings as well as the equivalent-circuit inductances has been discussed in [13], so will not be repeated here.
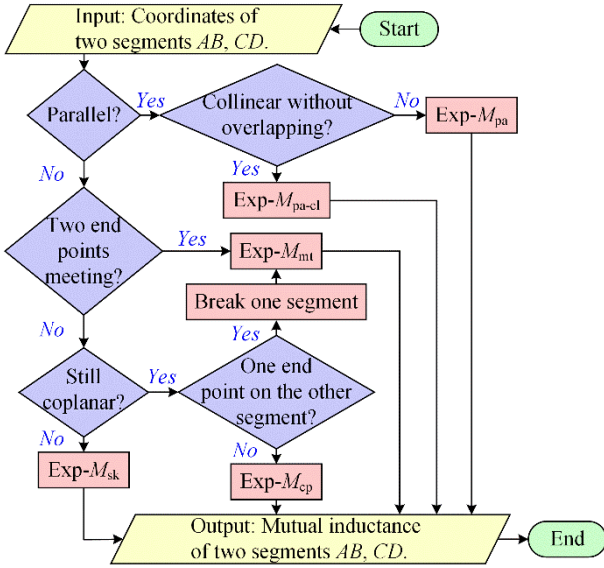

Fig. 7. Mutual inductance calculation procedure of two straight filamentary segments placed at any orientation in 3-D.

IV. 3-D FEA VALIDATION AND DISCUSSION

In this section, the proposed geometry modeling and inductance calculation method is validated on a three-phase, six-pole ACRIM design. The geometry parameters of the ACRIM used for validation are shown in Table I. In addition, the "neck" length in part JA is set as 1 mm for both stator and rotor, the axial length of part AE is set to 2.4 mm for stator and 2.15 mm for rotor.

Because $w_{ax,rot}/d_{ax,rot} \approx 5$, $w_{ax,stat}/d_{ax,rot} \approx 5$ and $d_{ax,stat}/d_{ax,rot} \approx 2$, rotor and stator coils are set to have 5-by-1 filaments and 5-by-2 filaments, respectively, in the analytic calculation. The analytic coil shapes are shown in Fig. 8(a) and (b). Fig. 8(c), (d) and (e) shows the full 3-D FEA model of both stator and

rotor three phase windings, symmetry is invoked so only half model is built to reduce the solution time. The proposed method is applicable to any rotor position, in this case the inductance is calculated when the stator and rotor axial windings of corresponding phases are geometrically aligned.

Table I
GEOMETRY PARAMETERS OF A THREE-PHASE, SIX-POLE ACRIM

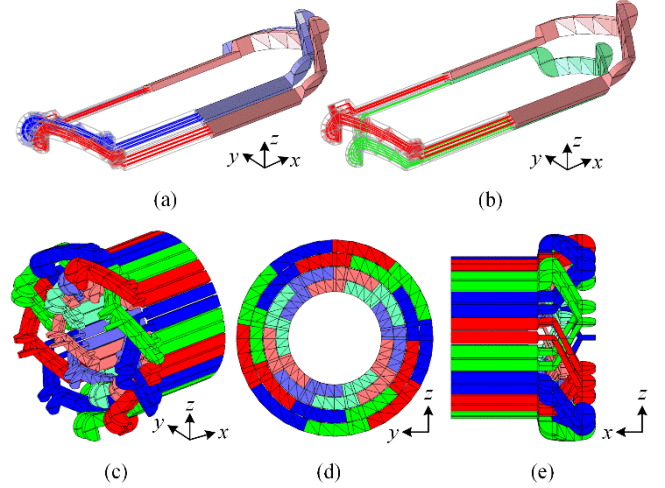|	Stator	Rotor
Number of coils per pole per-phase, q	2	2
Axial winding baseline circle radius, r_b	109.9 mm	103.3 mm
Axial coil side width (tangential), w_{ax}	16.68 mm	15.93 mm
Axial coil side depth (radial), d_{ax}	7.20 mm	3.50 mm
Axial winding length, h	240 mm	215 mm
End-winding coil side width (axial), w_{en}	7.20 mm	3.50 mm
End-winding coil side depth (radial), d_{en}	18.53 mm	17.70 mm
End-winding angle, φ	29.78°	27.28°

Fig. 8. (a) and (b) Analytic and 3-D FEA coils of the ACRIM design, (a) shows two adjacent stator coils and (b) shows one stator coil and one geometrically aligned rotor coil. (c), (d) and (e) Full 3-D FEA winding model.

The FEA inductance values are obtained by exciting one stator or rotor phase then calculating the fluxes linking all the phases. Fig. 9(a), (b), (c) and (d) show the 3-D FEA results of the ACRIM when stator phase A is excited. The field produced by the end-windings can be clearly observed in Fig. 9(a), (b) and (d). The red streamlines with arrows inside coils illustrate the excitation current; the arrows in space visualize the vector field of magnetic flux density. The 3-D FEA inductance values, are compared in Table II. The multi-filament method achieves good accuracy, most of the discrepancies are under 1% and the largest discrepancy of 2.06%.

Table II
COMPARISON OF THE ANALYTIC ESTIMATED AND 3-D FEA VALUES[1]

Unit	3-D FEA results μH	Multi-filament results μH	Discrepancy[2] (%)
L_{sA}	4.2399	4.2246	0.36
L_{ra}	3.5846	3.5938	−0.26
M_{AB}	−0.4305	−0.4246	1.36
M_{ab}	−0.4829	−0.4772	1.18
M_{Aa}	2.3329	2.3260	0.29
M_{Ab}	−0.4933	−0.4831	2.06
M_{Ac}	−0.4838	−0.4793	0.94
L_s	4.6704	4.6492	0.45
L_r	4.0675	4.0710	−0.09
M	2.8215	2.8072	0.50

[1] Stator and rotor windings are geometrically aligned.
[2] Discrepancies are calculated with respect to the 3-D FEA results.

where L_{sA} is the stator one phase (phase A) self-inductance; L_{ra} is the rotor one phase (phase a) self-inductance; M_{AB} is the

mutual inductance of stator phase A and B, i.e., the stator phase-to-phase mutual inductance; M_{ab} is the mutual inductance of rotor phase a and b, i.e., the rotor phase-to-phase mutual inductance. For a balanced three-phase winding, $M_{AB} = M_{AC}$ and $M_{ab} = M_{ac}$. M_{Aa} is the mutual inductance of stator phase A and rotor phase a, i.e., the stator-to-rotor homonym phase inductance; M_{Ab} and M_{Ac} are the mutual inductance of stator phase A and rotor phase b and rotor phase c respectively, i.e., the stator-to-rotor heteronym phase inductance. When stator phase A and rotor phase a are geometrically aligned, M_{Ab} and M_{Ac} may not have the same value, as shown in Table II, because the geometric alignment only refers to the axial windings, so magnetic alignment between stator and rotor phases are not necessarily ensured considering the complicated end-winding shapes with bending and twisting.

Table III compares the 2-D FEA and single-filament analytic inductance results with the values derived by 3-D FEA. In the single-filament method, the stator and rotor self-inductances are calculated by converting the original rectangular cross-section into an equivalent round cross-section which has the same area. The 2-D FEA magnetic flux density plot are shown in Fig. 9(e).

Table III
COMPARISON OF THE 2-D FEA RESULTS AND SINGLE-FILAMENT ANALYTIC ESTIMATION RESULTS WITH 3-D FEA RESULTS

| | 2-D FEA results | | Single-filament results | |
	Inductance (μH)	Discrepancy[*] (%)	Inductance (μH)	Discrepancy[*] (%)
L_{sA}	2.0565	51.50	4.3705	−3.08
L_{ra}	2.1390	40.33	3.8644	−7.81
M_{AB}	−0.6424	−49.21	−0.4106	4.61
M_{ab}	−0.6477	−34.14	−0.4609	4.55
M_{Aa}	1.7597	24.57	2.4214	−3.79
M_{Ab}	−0.6172	−25.12	−0.4727	4.16
M_{Ac}	−0.6172	−27.57	−0.4687	3.13
L_s	2.6989	42.21	4.7812	−2.37
L_r	2.7867	31.49	4.3254	−6.34
M	2.3769	15.76	2.8921	−2.50

[*] Discrepancies are calculated with respect to the 3-D FEA results.

The 2-D FEA results have a large discrepancy with respect to the 3-D results because it assumes infinite-long axial windings and ignores the end-windings. The single-filament method has a discrepancy level below 10% and most discrepancies are around 5%, which is larger than the multi-filament results, but still shows a reasonably good accuracy compared to 2-D FEA values, because the analytic coils have a high fidelity to 3-D FE coils. Both the single-filament and multi-filament methods greatly reduce the solution time compared to 3-D FEA, as shown in Table IV.

Table IV
COMPARISON OF THE SOLUTION TIME[*]

| | FE methods | | Analytic methods | |
Solution Time	3-D FEA	2-D FEA	Single-filament	Multi-filament
	28 min 39 s	10 s	2 s	59 s

[*] Computations are carried out on a PC with a 3.20 GHz CPU and 16 GB RAM.

V. CONCLUSION

This paper proposes a combined geometry modeling and 3-D inductance calculation method for ACRIMs. The geometry construction process can handle coils with non-circular cross-sections and complex shapes. Coils are firstly characterized by a series of cross-sections then discretized using straight filamentary segments. The cross-section shape, conductor bending and twisting can be reflected by the spatial arrangement of multi-filaments. The calculated coordinates of coils can be used directly to build a 3-D FEA model. The inductance calculation method uses closed-form solutions of Neumann integrals which is fast, accurate and robust so is suitable to be incorporated into an optimization program. The calculation procedure for mutual inductance of two straight segments placed at any orientation in 3-D is explained. The comparison between analytic estimated and 3-D FEA results shows the proposed method achieves a good accuracy, which also confirms the importance of a high-fidelity geometry modeling.
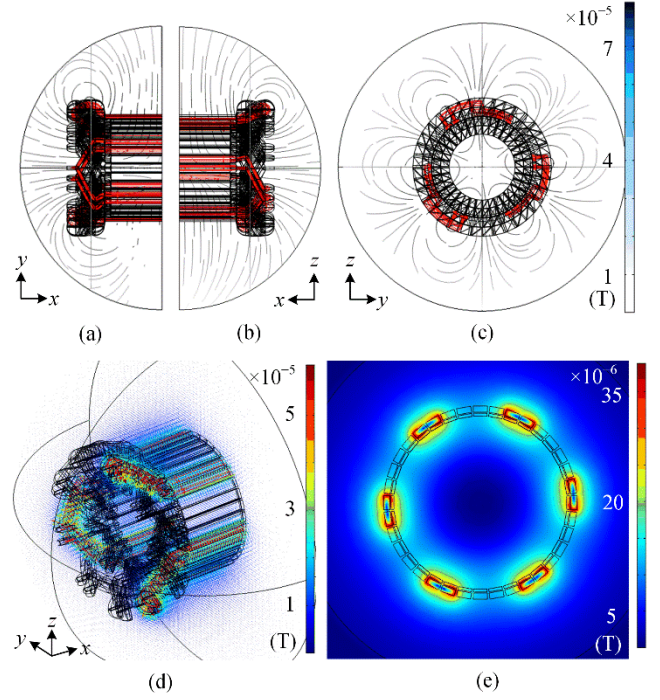

Fig. 9. (a), (b), (c) and (d) 3-D FEA results when stator phase A is excited by 1 A current. Red streamlines illustrate the stator phase A excitation current; arrows plot the magnetic flux density. (e) 2-D FEA magnetic flux density plot when stator phase A is excited by 1 A current.

APPENDIX

Closed-form solutions for mutual inductance of two straight segments have been derived in [10], they are presented here for clearness of explanation in Section III-A and for any practical purposes. For expressions in this section, the unit for length is meter and the unit of inductance is henry.

A. Mutual Inductance of Two Parallel Segments

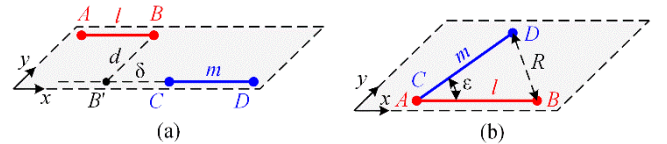Two parallel segments are shown in Fig. 10(a), the mutual inductance of them, M_{pa}, is (7).

Fig. 10. (a) Two parallel segments. B' is the projection of B on CD, $|BB'|=d$, $|CB'|=|\delta|$. (b) Two segments meeting at one end. $|DB| = R$, $\angle BAD = \varepsilon$.

$$M_{pa} = 10^{-7}(\alpha \sinh^{-1}(\alpha/d) - \beta \sinh^{-1}(\beta/d)$$
$$-\gamma \sinh^{-1}(\gamma/d) + \delta \sinh^{-1}(\delta/d) - \sqrt{\alpha^2 + d^2} \qquad (7)$$
$$+\sqrt{\beta^2 + d^2} + \sqrt{\gamma^2 + d^2} - \sqrt{\delta^2 + d^2})$$

where $\alpha = l+m+\delta$, $\beta = l+\delta$, $\gamma = m+\delta$, and d is the distance between two segments so is always positive, while δ can be a negative number. Singularity issue arises when $d = 0$, and (1) needs to be applied instead for non-overlapping segments.

B. Mutual Inductance of Two Unparallel Segments Meeting at One End

Fig. 10(b) shows two segments unparallel and meeting at one end, the mutual inductance of them, M_{mt}, is (8).

$$M_{mt} = 2 \times 10^{-7} \cos \varepsilon (l \tanh^{-1}(m/(l+R)) \\ + m \tanh^{-1}(l/(m+R))) \tag{8}$$

According to the geometry relation in Fig. 10(b) and triangle inequality, $m < l+R$, $l < m+R$, so applying (8) to end-meeting unparallel segments does not encounter singularities.

C. Mutual Inductance of Two Unparallel But Coplanar Segments Without Two End-Points Meeting

Two unparallel but coplanar segments without end-point meeting are shown in Fig. 11(a), the mutual inductance of them, M_{cp}, is (9).

(a)   (b)
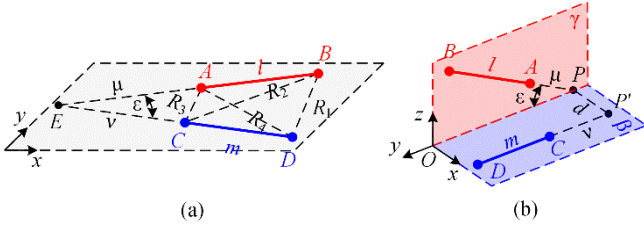
Fig. 11. (a) Two unparallel but coplanar segments without end-point meeting. E is the point of intersection of (the extensions of) AB and CD. $|AE|=\mu$, $|CE|=\nu$, $|BD|=R_1$, $|BC|=R_2$, $|AC|=R_3$, $|AD|=R_4$, $\angle AEC = \varepsilon$. (b) Two skew segments. AB is on plane γ, CD is on plane β, and $\beta \perp \gamma$, OP is the line of intersection of β and γ, $|PP'|=d$, $|CB|=\nu$, $|AP|=\mu$, $\angle BPO = \varepsilon$, and $|BD|=R_1$, $|BC|=R_2$, $|AC|=R_3$, $|AD|=R_4$.

$$M_{cp} = 2 \times 10^{-7} \cos \varepsilon ((\mu+l) \tanh^{-1}(m/(R_1 + R_2)) \\ + (\nu+m) \tanh^{-1}(l/(R_1 + R_4)) \\ - \mu \tanh^{-1}(m/(R_3 + R_4)) - \nu \tanh^{-1}(l/(R_2 + R_3)) \tag{9}$$

where $\alpha^2 = R_4^2 - R_3^2 + R_2^2 - R_1^2$, $\cos \varepsilon = \alpha^2/(2lm)$, and

$$\mu = \frac{(2m^2(R_2^2 - R_3^2 - l^2) + \alpha^2(R_4^2 - R_3^2 - m^2))l}{4l^2m^2 - \alpha^4} \tag{10}$$

$$\nu = \frac{(2l^2(R_4^2 - R_3^2 - m^2) + \alpha^2(R_2^2 - R_3^2 - l^2))m}{4l^2m^2 - \alpha^4} \tag{11}$$

The expression is not applicable to the situation when $R_1+R_2 = m$, or $R_1+R_4 = l$, or $R_3+R_4 = m$, or $R_2+R_3 = l$.

D. Mutual Inductance of Skew Segments

Two skew segments are shown in Fig. 11(b), the mutual inductance of them, M_{sk}, is (12).

$$M_{sk} = \text{Exp-}M_{cp} - 10^{-7} \Omega d \cos \varepsilon / \sin \varepsilon \tag{12}$$

The first term in (12) has the same expression as (9) so is abbreviated as Exp-M_{cp}. In (12). Also, there are $\alpha^2 = R_4^2 - R_3^2$

$+ R_2^2 - R_1^2$, $\cos \varepsilon = \alpha^2/(2lm)$, and the expressions of μ, ν are the same as (10) and (11). Besides, $d^2 = R_3^2 - \mu^2 - \nu^2 + 2\mu\nu\cos \varepsilon$. The term Ω is calculated as

$$\Omega = \tan^{-1}\left(\frac{d^2 \cos \varepsilon + (\mu+l)(\nu+m)\sin^2 \varepsilon}{dR_1 \sin \varepsilon} \right) \\ - \tan^{-1}\left((d^2 \cos \varepsilon + (\mu+l)\nu \sin^2 \varepsilon) / (dR_2 \sin \varepsilon) \right) \\ + \tan^{-1}\left((d^2 \cos \varepsilon + \mu\nu \sin^2 \varepsilon) / (dR_3 \sin \varepsilon) \right) \\ - \tan^{-1}\left((d^2 \cos \varepsilon + \mu(\nu+m) \sin^2 \varepsilon) / (dR_4 \sin \varepsilon) \right) \tag{13}$$

According to the geometry relation, $R_1 + R_2 > m$, $R_1 + R_4 > l$, $R_3 + R_4 > m$, and $R_2 + R_3 > l$. $d > 0$, $\varepsilon \neq 0$ and $\varepsilon \neq \pi$, so singularity issue does not occur when applying this expression to two skew segments.

REFERENCES

[1] M. F. Iacchetti, R. P. Deodhar, A. C. Smith and K. Mishima, "Modelling and operating characteristics of air-cored resonant induction machines," in *Proc. IEEE Energy Convers. Congr. Expo.*, 2018, pp. 6468-6475.

[2] Z. Jin et al., "Air-Cored Resonant Induction Machines: Comparison of Capacitor Tuning Criteria and Experimental Validation," in *IEEE Trans. Ind. Appl.*, vol. 57, no. 4, pp. 3595-3606, July-Aug. 2021

[3] B. J. Ebot and Y. Fuiimoto, "A general framework for the analysis and design of a wireless resonant motor," in *Proc. IEEE Int. Elect. Mach. Drives Conf.*, 2019, pp. 1966–1970.

[4] K. Sakai and K. Takijima, "Basic design of an ultra-lightweight machine based on magnetic resonance coupling and influence of AC losses due to high frequency," in *Proc. IEEE Energy Convers. Congr. Expo.*, 2019, pp. 3010-3016.

[5] M. Liu, K. W. Chan, J. Hu, Q. Lin, J. Liu and W. Xu, "Design and realization of a coreless and magnetless electric motor using magnetic resonant coupling technology," in *IEEE Trans. Energy Convers.*, vol. 34, no. 3, pp. 1200-1212, Sept. 2019.

[6] Z. Zhang, A. Matveev, R. Nilssen and A. Nysveen, "Ironless permanent-magnet generators for offshore wind turbines," in *IEEE Trans. Ind. Appl.*, vol. 50, no. 3, pp. 1835-1846, May-June 2014.

[7] N. Taran, D. M. Ionel and D. G. Dorrell, "Two-level surrogate-assisted differential evolution multi-objective optimization of electric machines using 3-D FEA," in *IEEE Trans. Magn.*, vol. 54, no. 11, pp. 1-5, Nov. 2018.

[8] F. Maurer, B. Kawkabani and J. K. Nøland, "Rapid 3-D magnetic integral field computation of current-carrying finite arc segments with rectangular cross section," in *IEEE Trans. Magn.*, vol. 56, no. 2, pp. 1-12, Feb. 2020.

[9] A. Smith and S. Williamson, "End-winding leakage reactance of concentrically-wound machines," in *Proc. Int. Conf. on Elect. Mach.*, 2002, pp. 64–69.

[10] F. W. Grover, *Inductance calculations: Working Formulas and Tables*. Chelmsford, MA, USA: Courier Corporation, 2004.

[11] D. Ban, D. Zarko and I. Mandic, "Turbogenerator end-winding leakage inductance calculation using a 3-D analytical approach based on the solution of Neumann Integrals," in *IEEE Trans. Energy Convers.*, vol. 20, no. 1, pp. 98-105, March 2005.

[12] E. Angel and D. Shreiner, *Interactive computer graphics: a top-down approach with WebGL*. Boston, MA, USA: Pearson, 2014.

[13] Z. Jin et al., "A Fast 3-D Winding Inductance Estimation Method for Air-Cored Resonant Induction Machines," in *IEEE Trans. Ind. Appl.*, Early Access, 2022.

[14] Ansys® Electromagnetics Suite, 2019 R3.7, Maxwell and RMxprt help, ANSYS, Inc.